Close to transform-limited, few-cycle 12 µJ pulses at 400 kHz for applications in ultrafast spectroscopy

Federico J. Furch,[1,*] **Achut Giree,**[1,2] **Felipe Morales,**[1] **Alexandria Anderson,**[1] **Yicheng Wang,**[1] **Claus Peter Schulz,**[1] **and Marc J. J. Vrakking**[1]

[1]*Max Born Institute, Max-Born-Straße 2A, D12489, Berlin, Germany.*
[2]*Amplitude Technologies, 2-4 rue du Bois Chaland - CE 2926, 91029 Évry, France.*
*furch@mbi-berlin.de

Abstract: Non-collinear Optical Parametric Amplification has become the leading technology for amplifying few-cycle Carrier-Envelope Phase (CEP) stable pulses to high energy at extreme repetition rates. In this work, a parametric amplifier system devoted to ultrafast photoionization experiments with coincidence detection is reported. The amplifier delivers CEP-stable few-cycle pulses with an average power of 5 W, and operates at repetition rates between 400 and 800 kHz. Close to transform-limited compression of the few-cycle pulses is achieved with minimized spatio-temporal distortions. Potential limitations introduced by spatio-temporal couplings to applications in attosecond science are analyzed. In particular, it is shown that pulse front tilt resulting from non-collinear amplification can considerably reduce the asymmetry in stereo above threshold ionization (stereo-ATI) experiments.

References and Links

1. F. Krausz and M. Ivanov, "Attosecond physics," Rev. Mod. Phys. **81**, 163-234 (2009).
2. M. Drescher, M. Hentschel, R. Kienberger, M. Uiberacker, V. Yakovlev, A. Scrinzi, T. Westerwalbesloh, U. Kleineberg, U. Heinzmann, and F. Krausz, "Time-resolved atomic inner-shell spectroscopy," Nature **419**, 803-807 (2002)
3. M. F. Kling, C. Siedschlag, A. J. Verhoef, J. I. Khan, M. Schultze, T. Uphues, Y. Ni, M. Uiberacker, M. Drescher, F. Krausz, and M. J. J. Vrakking, "Control of electron localization in molecular dissociation," Science **312**, 246-248 (2006).
4. G. Sansone, F. Kelkensberg, J. F. Perez-Torres, F. Morales, M. F. Kling, W. Siu, O. Ghafur, P. Johnsson, M. Swoboda, E. Benedetti, F. Ferrari, F. Lepine, J. L. Sanz-Vicario, S. Zherebtsov, I. Znakovskaya, A. L'Huillier, M. Y. Ivanov, M. Nisoli, F. Martín, and M. J. J. Vrakking, "Electron localization following attosecond molecular photoionization," Nature **465**, 763-767 (2010).
5. E. Goulielmakis, Z.-H. Loh, A. Wirth, R. Santra, N. Rohringer, V. S. Yakovlev, S. Zherebtsov, T. Pfeifer, A. M. Azzeer, M. F. Kling, S. R. Leone, and F. Krausz, "Real-time observation of valence electron motion," Nature **466**, 739-743 (2010).
6. D. W. Chandler and P. L. Houston, "Two-dimensional imaging of state-selected photodissociation products detected by multiphoton ionization," J. Chem. Phys. **87**, 1445-1447 (1987).
7. O. Ghafur, W. Siu, P. Johnsson, M. F. Kling, M. Drescher, and M. J. J. Vrakking, "A velocity map imaging detector with an integrated gas injection system," Rev. Sci. Instrum. **80**, 033110 (2009).
8. R. Dörner, V. Mergel, O. Jagutzki, L. Spielberger, J. Ullrich, R. Moshammer, and H. Schmidt-Böcking, "Cold target recoil ion momentum spectroscopy: a 'momentum microscope' to view atomic collision dynamics," Phys. Rep. **330**, 95-192 (2000).
9. J. Ullrich, R. Moshammer, A. Dorn, R. Dörner, L. P. H. Schmidt, and H. Schmidt-Böcking, "Recoil-ion and electron momentum spectroscopy: reaction-microscopes," Rep. Prog. Phys. **66**, 1463-1545 (2003).
10. A. Fischer, A. Sperl, P. Cörlin, M. Schönwald, H. Rietz, A. Palacios, A. González-Castrillo, F. Martín, T. Pfeifer, J. Ullrich, A. Senftleben, and R. Moshammer, "Electron localization involving doubly excited states in broadband extreme ultraviolet ionization of H_2," Phys. Rev. Lett. **110**, 213002 (2013).
11. M. Sabbar, S. Heuser, R. Boge, M. Lucchini, L. Gallmann, C. Cirelli, and U. Keller, "Combining attosecond XUV pulses with coincidence spectroscopy," Rev. Sci. Instrum. **85**, 103113 (2014).

12. B. Bergues, M. Kubel, N. G. Johnson, B. Fischer, N. Camus, K. J. Betsch, O. Herrwerth, A. Senftleben, A. M. Sayler, T. Rathje, T. Pfeifer, I. Ben-Itzhak, R. R. Jones, G. G. Paulus, F. Krausz, R. Moshammer, J. Ullrich, and M. F. Kling, "Attosecond tracing of correlated electron-emission in non-sequential double ionization," Nat. Commun. **3**, 813 (2012).

13. N. Camus, B. Fischer, M. Kremer, V. Sharma, A. Rudenko, B. Bergues, M. Kubel, N. G. Johnson, M. F. Kling, T. Pfeifer, J. Ullrich, and R. Moshammer, "Attosecond Correlated Dynamics of Two Electrons Passing through a Transition State," Phys. Rev. Lett. **108**, 073003 (2012).

14. B. Gaire, D. J. Haxton, F. P. Sturm, J. Williams, A. Gatton, I. Bocharova, N. Gehrken, M. Schoffler, H. Gassert, S. Zeller, J. Voigtsberger, T. Jahnke, M. Zohrabi, D. Reedy, C. Nook, A. L. Landers, A. Belkacem, C. L. Cocke, I. Ben-Itzhak, R. Dörner, and T. Weber, "Auger decay and subsequent fragmentation pathways of ethylene following K-shell ionization," Phys. Rev. A **92**, 013408 (2015).

15. L. Zhang, X. H. Xie, S. Roither, D. Kartashov, Y. L. Wang, C. L. Wang, M. Schoffler, D. Shafir, P. B. Corkum, A. Baltuška, I. Ivanov, A. Kheifets, X. J. Liu, A. Staudte, and M. Kitzler, "Laser-sub-cycle two-dimensional electron-momentum mapping using orthogonal two-color fields," Phys. Rev. A **90**, 061401 (2014).

16. G. Cerullo, M. Nisoli, S. Stagira, and S. De Silvestri, "Sub-8-fs pulses from an ultrabroadband optical parametric amplifier in the visible," Opt. Lett. **23**, 1283-1285 (1998).

17. A. Shirakawa, I. Sakane, M. Takasaka, and T. Kobayashi, "Sub-5-fs visible pulse generation by pulse-front-matched noncollinear optical parametric amplification," App. Phys. Lett. **74**, 2268-2270 (1999).

18. R. Riedel, J. Rothhardt, K. Beil, B. Gronloh, A. Klenke, H. Höppner, M. Schulz, U. Teubner, C. Kränkel, J. Limpert, A. Tünnermann, M. J. Prandolini, and F. Tavella, "Thermal properties of borate crystals for high power optical parametric chirped-pulse amplification," Opt. Express **22**, 17607-17619 (2014).

19. E. Innerhofer, T. Südmeyer, F. Brunner, R. Häring, A. Aschwanden, R. Paschotta, C. Hönninger, M. Kumkar, and U. Keller, "60-W average power in 810-fs pulses from a thin-disk Yb:YAG laser," Opt. Lett. **28**, 367-369 (2003).

20. P. Russbueldt, T. Mans, G. Rotarius, J. Weitenberg, H. D. Hoffmann, and R. Poprawe, "400 W Yb:YAG innoslab fs-amplifier," Opt. Express **17**, 12230-12245 (2009).

21. T. Eidam, S. Hanf, E. Seise, T. V. Andersen, T. Gabler, C. Wirth, T. Schreiber, J. Limpert, and A. Tünnermann, "Femtosecond fiber CPA system emitting 830 W average output power," Opt. Lett. **35**, 94-96 (2010).

22. B. A. Reagan, K. A. Wernsing, A. H. Curtis, F. J. Furch, B. M. Luther, D. Patel, C. S. Menoni, and J. J. Rocca, "Demonstration of a 100 Hz repetition rate gain-saturated diode-pumped table-top soft x-ray laser," Opt. Lett. **37**, 3624-3626 (2012).

23. D. E. Miller, L. E. Zapata, D. J. Ripin, and T. Y. Fan, "Sub-picosecond pulses at 100 W average power from a Yb:YLF chirped-pulse amplification system," Opt. Lett. **37**, 2700-2702 (2012).

24. L. E. Zapata, F. Reichert, M. Hemmer, and F. X. Kärtner, "250 W average power, 100 kHz repetition rate cryogenic Yb:YAG amplifier for OPCPA pumping," Opt. Lett. **41**, 492-495 (2016).

25. J. Rothhardt, S. Demmler, S. Hädrich, J. Limpert, and A. Tünnermann, "Octave-spanning OPCPA system delivering CEP-stable few-cycle pulses and 22 W of average power at 1 MHz repetition rate," Opt. Express **20**, 10870-10878 (2012).

26. M. Puppin, Y. P. Deng, O. Prochnow, J. Ahrens, T. Binhammer, U. Morgner, M. Krenz, M. Wolf, and R. Ernstorfer, "500 kHz OPCPA delivering tunable sub-20 fs pulses with 15 W average power based on an all-ytterbium laser," Opt. Express **23**, 1491-1497 (2015).

27. S. Prinz, M. Haefner, C. Y. Teisset, R. Bessing, K. Michel, Y. Lee, X. T. Geng, S. Kim, D. E. Kim, T. Metzger, and M. Schultze, "CEP-stable, sub-6 fs, 300-kHz OPCPA system with more than 15 W of average power," Opt. Express **23**, 1388-1394 (2015).

28. J. Matyschok, T. Lang, T. Binhammer, O. Prochnow, S. Rausch, M. Schultze, A. Harth, P. Rudawski, C. L. Arnold, A. L'Huillier, and U. Morgner, "Temporal and spatial effects inside a compact and CEP stabilized, few-cycle OPCPA system at high repetition rates," Opt. Express **21**, 29656-29665 (2013).

29. J. Biegert, P. K. Bates, and O. Chalus, "New Mid-Infrared Light Sources," IEEE J. Sel. Top. Quantum Elec. **18**, 531-540 (2012).

30. B. W. Mayer, C. R. Phillips, L. Gallmann, M. M. Fejer, and U. Keller, "Sub-four-cycle laser pulses directly from a high-repetition-rate optical parametric chirped-pulse amplifier at 3.4 μm," Opt. Lett. **38**, 4265-4268 (2013).

31. M. Mero, F. Noack, F. Bach, V. Petrov, and M. J. J. Vrakking, "High-average-power, 50-fs parametric amplifier front-end at 1.55 μm," Opt. Express **23**, 33157-33163 (2015).

32. P. Rudawski, A. Harth, C. Guo, E. Lorek, M. Miranda, C. M. Heyl, E. W. Larsen, J. Ahrens, O. Prochnow, T. Binhammer, U. Morgner, J. Mauritsson, A. L'Huillier, and C. L. Arnold, "Carrier-envelope phase dependent high-order harmonic generation with a high-repetition rate OPCPA-system," Eur. Phys. J. D **69**, 70 (2015).

33. M. Krebs, S. Hädrich, S. Demmler, J. Rothhardt, A. Zair, L. Chipperfield, J. Limpert, and A. Tünnermann, "Towards isolated attosecond pulses at megahertz repetition rates," Nat. Photonics **7**, 555-559 (2013).

34. F. J. Furch, S. Birkner, F. Kelkensberg, A. Giree, A. Anderson, C. P. Schulz, and M. J. J. Vrakking, "Carrier-envelope phase stable few-cycle pulses at 400 kHz for electron-ion coincidence experiments," Opt. Express **21**, 22671-22682 (2013).

35. J. Bromage, J. Rothhardt, S. Hadrich, C. Dorrer, C. Jocher, S. Demmler, J. Limpert, A. Tunnermann, and J. D. Zuegel, "Analysis and suppression of parasitic processes in noncollinear optical parametric amplifiers," Opt. Express **19**, 16797-16808 (2011).

36. J. Bromage, C. Dorrer, and J. D. Zuegel, "Performance Trade-Offs for High-Repetition-Rate Noncollinear Optical Parametric Amplifiers," in Lasers, Sources and Related Photonic Devices, OSA Technical Digest Series (CD) (Optical Society of America, 2010), paper ATuA23.
37. M. Kakehata, H. Takada, Y. Kobayashi, K. Torizuka, Y. Fujihira, T. Homma, and H. Takahashi, "Single-shot measurement of carrier-envelope phase changes by spectral interferometry," Opt. Lett. **26**, 1436-1438 (2001).
38. S. Hädrich, J. Rothhardt, M. Krebs, S. Demmler, J. Limpert, and A. Tünnermann, "Improving carrier-envelope phase stability in optical parametric chirped-pulse amplifiers by control of timing jitter," Opt. Lett. **37**, 4910-4912 (2012).
39. D. N. Schimpf, J. Rothhardt, J. Limpert, A. Ttinnermann, and D. C. Hanna, "Theoretical analysis of the gain bandwidth for noncollinear parametric amplification of ultrafast pulses," J. Opt. Soc. Am. B **24**, 2837-2846 (2007).
40. J. Bromage, C. Dorrer, and J. D. Zuegel, "Angular-dispersion-induced spatiotemporal aberrations in noncollinear optical parametric amplifiers," Opt. Letters **35**, 2251-2253 (2010).
41. A. Zaukevicius, V. Jukna, R. Antipenkov, V. Martinenaite, A. Varanavicius, A. Varanavicius, A. P. Piskarskas, and G. Valiulis, "Manifestation of spatial chirp in femtosecond noncollinear optical parametric chirped-pulse amplifier," J. Opt. Soc. Am. B **28**, 2902-2908 (2011).
42. T. Lang, A. Harth, J. Matyschok, T. Binhammer, M. Schultze, and U. Morgner, "Impact of temporal, spatial and cascaded effects on the pulse formation in ultra-broadband parametric amplifiers," Opt. Express **21**, 949-959 (2013).
43. A. Giree, F.J. Furch, M. Mero, G. Arisholm, M.J.J. Vrakking, "Analysis of Spatiotemporal Couplings in Noncollinear Optical Parametric Chirped-Pulse Amplifiers," in Conference on Lasers and Electro-Optics, OSA Technical Digest (2016) (Optical Society of America, 2016), paper SF2I.7.
44. J. Bromage, C. Dorrer, and J. D. Zuegel, "High-Resolution Spatio-Spectral Characterization of Noncollinear Optical Parametric Amplifiers," in Lasers, Sources and Related Photonic Devices, OSA Technical Digest Series (CD) (Optical Society of America, 2010), paper AME5.
45. P. Bowlan, P. Gabolde, M. A. Coughlan, R. Trebino, and R. J. Levis, "Measuring the spatiotemporal electric field of ultrashort pulses with high spatial and spectral resolution," J. Opt. Soc. Am. B **25**, A81-A92 (2008).
46. M. Miranda, M. Kotur, P. Rudawski, C. Guo, A. Harth, A. L'Huillier, and C. L. Arnold, "Spatiotemporal characterization of ultrashort laser pulses using spatially resolved Fourier transform spectrometry," Opt. Lett. **39**, 5142-5145 (2014).
47. T. Witting, S. J. Weber, J. W. G. Tisch, and J. P. Marangos, "Spatio-temporal characterization of mid-infrared laser pulses with spatially encoded spectral shearing interferometry," Opt. Express **20**, 27974-27980 (2012).
48. G. G. Paulus, F. Lindner, H. Walther, A. Baltuška, E. Goulielmakis, M. Lezius, and F. Krausz, "Measurement of the phase of few-cycle laser pulses," Phys. Rev. Lett. **91**, 253004 (2003).
49. G. G. Paulus, W. Nicklich, H. Xu, P. Lambropoulos, and H. Walther, "Plateau in above threshold ionization spectra," Phys. Rev. Lett. **72**, 2851-2854 (1994).
50. F. Lindner, G. G. Paulus, H. Walther, A. Baltuška, E. Goulielmakis, M. Lezius, and F. Krausz, "Gouy Phase Shift for Few-Cycle Laser Pulses," Phys. Rev. Lett. **92**, 113001 (2004).
51. H. G. Muller, "An efficient propagation scheme for the time-dependent Schrödinger equation in the velocity gauge," Laser Phys. **9**, 138-148 (1999).

1. Introduction

Ultrafast lasers with pulse durations in the femtosecond regime have found widespread use in the industrial and scientific communities, enabling new applications and research opportunities. In particular, the availability of CEP-stable few-cycle pulses with high energy in the visible and near infrared regions of the electromagnetic spectrum, has paved the way for the growing field of attosecond science (see for example [1-5]).

Current attosecond experiments rely most commonly on strong field ionization of matter with strong ultra-short infrared (IR) laser fields, or on two-colour pump-probe experiments combining synchronized extreme ultra-violet (XUV) pulses with attosecond duration produced through high harmonic generation and few-cycle IR pulses. In both cases, the velocity distribution of ions or electrons produced during photoionization is often recorded with either time-of-flight or velocity map imaging spectrometers [6, 7]. Another technique is the measurement of the transient absorption spectrum of an attosecond pulse at different times after excitation by a strong IR field. This has allowed, for example, accessing the evolution of bound excited states [5]. Despite impressive progress in the last decade, even the interpretation of results from simple experiments remains very challenging. Experiments in attosecond science often involve a complex scenario that may include excitation of multiple electronic states, electron-electron correlations and, in the case of molecules, coupling

between electronic and nuclear degrees of freedom. Electron-ion coincidence detection in a reaction microscope [8, 9] can provide correlated momentum distributions of ions and electrons and as a consequence, a more insightful picture of the photoionization process. Coincidence detection is becoming increasingly often the detection technique of choice for experiments in attosecond science [10-15].

Coincidence detection requires that the detected ions and electrons originate from the same parent atom or molecule. In order to establish a one to one correspondence between the charged particles detected and a parent atom or molecule, there must be only one ionization event per laser shot. In practice, this condition imposes the requirement of operating at an ionization rate of only a small fraction of the laser repetition rate. Therefore, detection in coincidence demands light sources with extremely high repetition rates. In this context non-collinear optical parametric amplifiers (NOPAs) are becoming very attractive for the attosecond science community. NOPAs allow efficient amplification of broadband pulses [16, 17]. Since thermal effects are to a considerable extent negligible during parametric amplification [18], the average power limitation due to thermal effects is passed on to the pump laser, where Yb-based amplifiers can provide few-picosecond and sub-picosecond pulses with high energy at extremely high average powers [19-24]. Current high average power broadband sources based on NOPAs cover repetition rates from a few hundred kHz to a few MHz, pulse energies up to several tens of μJ and pulse durations down to the few-cycle limit [25-31]. Moreover, it has been possible to demonstrate high harmonic generation and isolated attosecond XUV pulse generation utilizing these sources [32, 33].

Recently we introduced a first version of a new parametric amplification system. With a pump laser providing 12 W of power at 515 nm, we demonstrated amplification of CEP-stable few-cycle pulses from a Ti:Sapphire oscillator to 5 μJ at 400 kHz [34]. Additionally, the few-cycle pulses from this NOPA were utilized in a proof-of-principle strong field ionization experiment with coincidence detection, utilizing a home-built reaction microscope.

In this work we present a significant upgrade to our parametric amplifier system based on a new, more powerful pump laser, along with the implementation of pulse shaping for improved compression. We focus on the performance of the system in strong field ionization experiments with few-cycle pulses.

2. Amplifier setup

The box diagram in Fig. 1(a) presents schematically the newly developed NOPA. As in our previous system, a Ti:Sapphire oscillator (Pulse:ONE, VENTEON Femtosecond Laser Technologies GmbH) is used to seed the NOPA and the pump laser, in a passive synchronization scheme. The pump laser is an Yb-doped fiber-based Chirped Pulse Amplification (CPA) system (High Power Tangerine, Amplitude Systèmes) with a central wavelength around 1030 nm. To pump the NOPA, the output of the CPA is frequency-doubled. More than 24 W of power at 515 nm are delivered after second harmonic generation (SHG), in pulses with an approximate duration of 300 fs. The pulse energy depends on the repetition rate, which can be varied between 400 kHz and 800 kHz without the need of changing beam characteristics or crystal thickness in the SHG module. The CPA can be operated at higher repetition rates, but then the conversion efficiency in the SHG module starts dropping significantly due to the decreased pulse energy at constant average power. The repetition rate of the CPA determines the repetition rate of the NOPA, since only those pulses in the 80 MHz oscillator pulse train that overlap in time with the pulse train of the CPA will be amplified in the NOPA.
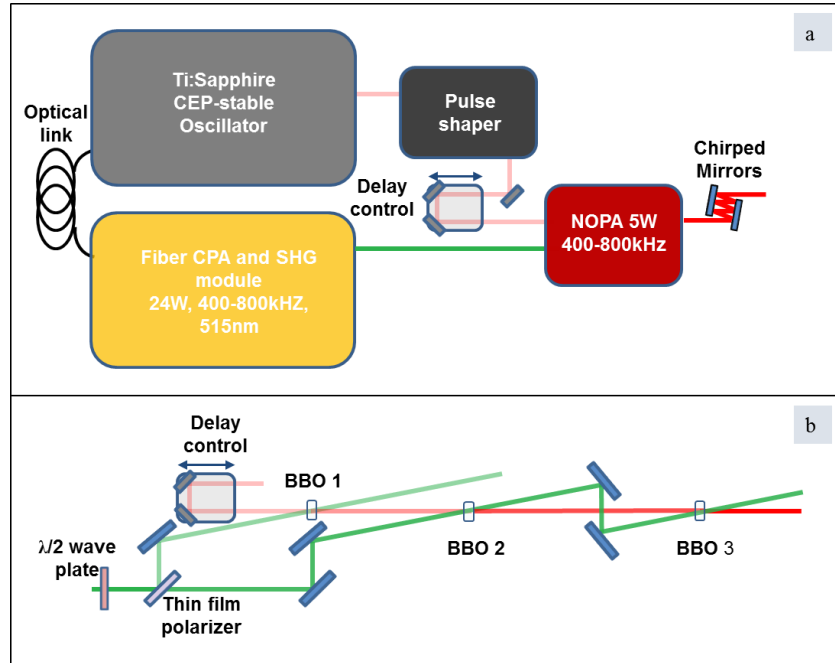
Fig. 1. (a) Block diagram of the amplifier system, delivering high repetition rate (400-800 kHz) CEP-stable few-cycle laser pulses at an average output power of 5 W. (b) Schematic of the NOPA.

The pump beam is split utilizing a wave plate and a polarizer in order to be able to pump a first and a second NOPA stage. Between 10% and 20% of the pump power is sent to the first stage (BBO 1 in Fig. 1(b)), depending on the repetition rate. The second stage divides the amplification process between two separate thin crystals (BBO 2 and BBO 3 in Fig. 1(b)). For the first stage a 2 mm thick BBO under type I phase-matching and walk-off compensation geometry was utilized to minimize spatio-temporal aberrations at the expense of small losses due to parasitic second harmonic generation of the signal (or seed) and idler pulses [35, 36]. In the second stage, BBO 2 has a thickness of 1.5 mm and is cut for walk-off compensation geometry. BBO 3 is either 1.5 or 2 mm thick (as will be discussed later) and cut for non-walk-off compensation geometry to minimize the losses due to parasitic second harmonic. The non-collinear angle in the first stage was set to approximately 2.5° (commonly referred to as the magic angle configuration) while in the second stage the non-collinear angles are slightly smaller (approximately 2.4°). The peak intensity of the pump pulses on the different BBO crystals varies between 250 GW/cm^2 in the first stage and 150 GW/cm^2 in the second stage. The ratio of seed pulse duration to pump pulse duration at the input face of BBO 1 was set to approximately 1/3.

In a first series of tests more than 120 mW of average power (1.5 nJ, 80 MHz) from the oscillator were sent into the first amplification stage to optimize and characterize the NOPA. Later on, a 4f-pulse shaper (MIIPS Box 640 P, Biophotonic Solutions Inc.) was incorporated into the seed path before the first amplification stage, in order to improve the compression of the pulses. In this case the incident power into the NOPA was reduced to less than 80 mW (1nJ, 80 MHz).

Although the pump and seed pulses are passively synchronized as described before, small changes in temperature over the long optical path inside the fiber CPA lead to slow changes in the delay between the pulses, which in turn translate into unstable output power and changing spectral shape of the NOPA over time. In order to overcome this issue, an active delay stabilization system was implemented. This is explained in more detail in section 4.

3. Amplifier performance at 400 kHz and 800 kHz

With the system configuration described in section 2, and with a thickness of BBO 3 of 2 mm, the performance of the amplifier was studied at 400 kHz and 800 kHz. Only the pump focusing into BBO 2 and the splitting ratio of the pump power was changed between operation at one or the other repetition rate. In both cases the power reaches 5 W (amplifier conversion efficiency from pump entering the NOPA to amplified signal, taking into account losses to parasitic second harmonic, of 21.5 %). That means that the amplifier can deliver pulse energies as high as 12.5 µJ when operated at 400 kHz. In these initial measurements the delay between pump and seed was not actively stabilized. Therefore the output power drifted away from the maximum value on a timescale of a few minutes. This drift was minimized by the incorporation of the active delay stabilization system described in the next section. In addition, the amplified optical parametric fluorescence (AOPF) measured when the seed into the NOPA was blocked resulted in less than 10% of the amplified signal power of the seeded amplifier in all configurations studied. The actual content of AOPF in the seeded amplified signal is much smaller given that the parasitic process is heavily suppressed in the presence of the seed.

In Fig. 2 the spectrum of the amplified pulses out of each of the three BBO crystals is presented for both repetition rates. The exact shape of the spectrum depends on many parameters including the pump intensity incident on each crystal, the non-collinear and phase matching angles and the delay between pump and seed.
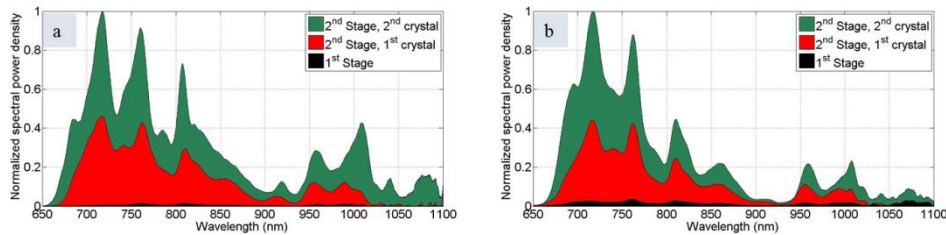

Fig. 2. Pulse spectrum out of each BBO crystal for (a) operation at 400 kHz and (b) operation at 800 kHz.

In both cases the amplified pulse spectrum supports sub-6 fs pulses. The pulses were compressed utilizing a pair of chirped mirrors and thin wedges. For both repetition rates compression to sub-9 fs pulses was achieved. This result was significantly improved with the implementation of optimized chirped mirrors and a pulse shaper, as it is shown in the next section.

The Ti:Sapphire oscillator is Carrier-Envelope Offset-frequency (CEO) stabilized. That means that the Carrier-Envelope Phase slip from pulse to pulse is constant. In this particular case, after 4 pulses in the 80 MHz pulse train the phase slip adds up to 2π. The repetition rate of the pump laser is then selected such that only pulses that carry the same CEP are amplified in the NOPA. The CEP stability after amplification was studied with a home-built f-to-2f interferometer, detecting the change over time in the phase of the modulation in a small part of the octave-spanning spectrum [37]. The minimum integration time in the spectrometer utilized was 2 ms and therefore each spectrum integrated 800 or 1600 pulses at 400 kHz and 800 kHz respectively. While this fact prevents one from properly quantifying the CEP stability, the almost full spectral modulation that is achieved in selected parts of the spectrum suggests that during the integration of the spectrum the change in the CEP is relatively small. A proper characterization of the CEP stability at these high repetition rates will be the subject of future investigations. Figure 3 shows spectral fringes as a function of time taken at 400 kHz. The fringes disappear when the CEO-locking system of the oscillator is turned off. Additionally, the delay stabilization system was turned on and off, and, as previously shown

in [38], the stability of the spectral fringes improves when the delay between pump and seed pulses in the NOPA is actively stabilized.
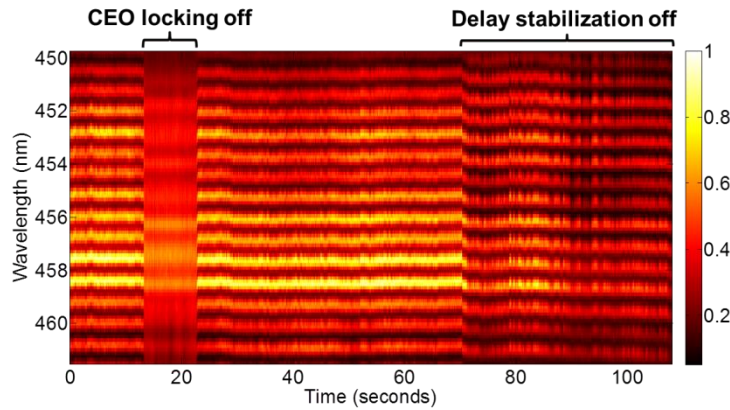

Fig. 3. Spectral fringes measured in the f-to-2f interferometer as a function of time while operating the parametric amplifier at 400 kHz.

4. System optimization for applications at 400 kHz

At least two points have to be considered when the system is utilized in applications. First of all, additional components such as wave plates have to be added after the amplifier to control the polarization, as well as combinations of half-wave plates and polarizers to continuously vary the energy on target, spectral filters to remove the parasitic second harmonic, windows at the input of vacuum chambers, etc. These additional optical elements make the pulse compression more challenging, and even if one could optimize the design of chirped mirrors for a particular application, the flexibility to change the experimental configuration would be lost. Second, the output power and peak power have to be stable over long periods of time. As mentioned in section 2, this requires active stabilization of the delay between the seed and pump pulses.

In order to overcome the difficulties in pulse compression, the optical path of the seed was rearranged to accommodate the pulse shaper mentioned in section 2, between the output of the oscillator and the entrance to the parametric amplifier. To minimize the changes in performance of the NOPA, a flat spectral phase was introduced initially. After amplification, the pulses were sent through a pair of chirped mirrors designed to compensate material dispersion in BBO, a pair of thin fused-silica wedges at Brewster´s angle, a broadband dispersion compensated neutral variable power attenuator (Femtolasers OA322), one dichroic mirror to separate the parasitic second harmonic from the fundamental, and propagated through fused silica windows and a few meters in air, to simulate the propagation of the pulse towards the interaction region for a particular experiment. The number of bounces on the chirped mirrors and the insertion of the thin wedges into the beam path were optimized to achieve the best compression possible. Subsequently, the compression was optimized by adjusting high order dispersion terms (up to 4th) with the pulse shaper, while monitoring the pulse duration.

The pulse duration was characterized with a SPIDER apparatus (FC-SPIDER, APE GmbH). Figure 4 shows a comparison between the retrieved pulse temporal shape and the transform-limited pulse shape. The retrieved pulse duration of 6.3 fs at full width at half maximum (FWHM) is only 1.09 times the transform-limited pulse duration. The pulse contrast against pre- and post-pulses is almost the same as the contrast of the transform-limited pulse temporal shape, and significantly improved over the pulse shape that we

reported in our earlier publication (i.e. before implementation of the pulse shaper), when at least half of the pulse energy was lost to post- and pre-pulses [34].
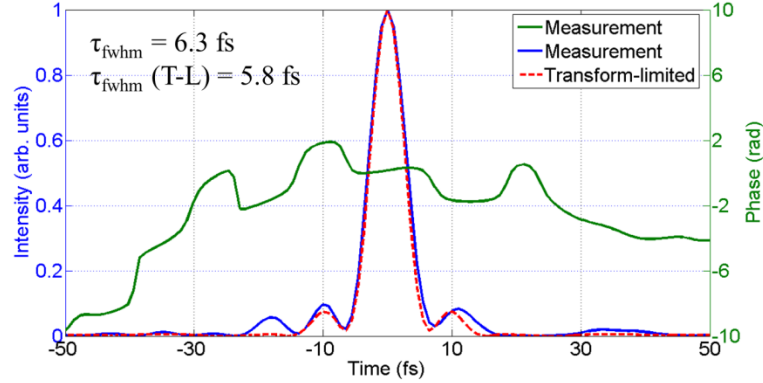

Fig. 4. Experimentally retrieved pulse shape through a SPIDER measurement (blue) and transform-limited pulse shape (red) obtained by Fourier transformation of the measured spectrum. The temporal phase from the SPIDER measurement is shown as well (green curve).

As already mentioned, to improve the system stability over extended periods of time, the delay between the seed and pump pulses in the NOPA was actively stabilized. In order to stabilize the delay, a measurement of the actual delay (or its change over time) is required. The idler from a parametric amplifier provides a cross correlation measurement between the seed and pump pulses, as can be corroborated by studying the coupled differential equations describing the amplification process [39]. The information contained in the idler was already utilized to stabilize the pump-seed delay in [38]. The same idea was followed here, utilizing the difference in signal between two photodiodes placed at two different portions of the angularly dispersed spectrum of the idler. Utilizing PID electronics to feed a motorized translation stage, the delay can be stabilized in order to preserve the spectral shape of the idler (and therefore the signal) over time. The main difference with respect to the work reported in [38] is that a separate NOPA stage was built for the purpose of stabilizing the delay. In that way, the stretching of the seed pulse can be tailored to optimize the sensitivity of the NOPA stage to changes in the delay, and not necessarily for the optimum seed pulse amplification. The idea of using a separate NOPA stage for delay stabilization was introduced in [27]. Unlike that particular system, where part of the total pump power (and seed power) is utilized for this separate stage, no splitting of pump (or seed) power was done in the system presented here. As a seed, a parasitic reflection off BBO 2 (refer to Fig. 1(b)) was utilized, and to pump the additional NOPA, the remaining pump power out of BBO 3 was used. A 5 mm thick BBO crystal under type I phase matching in walk-off compensation geometry was utilized to amplify the seed. The choice of crystal thickness was only determined by the available crystals in the laboratory at the time of setting up this additional NOPA. Thinner crystals would also work, as long as they provide enough idler power for the detection system. Figure 5 shows the influence of the active pump/seed stabilization system on the output power of the NOPA. The measurement was taken at the interaction region of a particular experiment after suffering considerable losses in several optical elements. Therefore the average power is lower than 5 W. The two different traces show the output power stability with and without the stabilization system. When the active stabilization system is functioning, the rms change in output power is less than 1 % over half an hour. Similar performance can be maintained over the course of many hours. The pulse-to-pulse stability was characterized with a fast photodiode and an oscilloscope. The voltage peak-to-peak was monitored over more than 6 minutes resulting in a standard deviation from the average value of approximately 3 %.
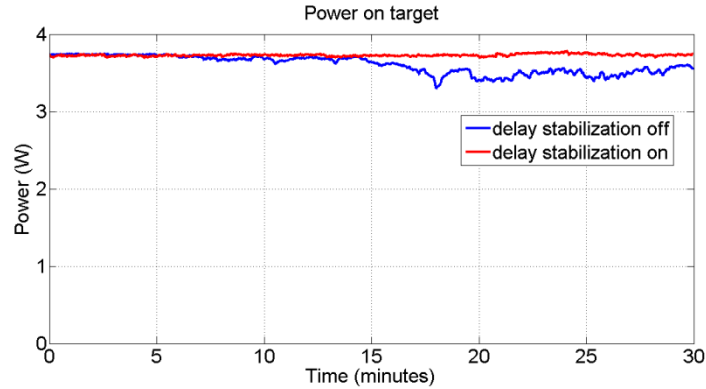
Fig. 5. NOPA output power with and without delay stabilization system.

5. Spatio-temporal aberrations

It is well known that the non-collinear configuration in parametric amplification may introduce strong couplings between spatial and temporal coordinates of the electromagnetic field [17, 36, 40-42]. To partially characterize these effects at the output of the NOPA, two techniques were utilized: SPIDER measurements were taken at different positions across the beam profile, and an imaging spectrograph was used to characterize the changes in the amplified spectrum as a function of position across one axis on the beam profile. The measurements with the imaging spectrograph were taken across the beams' walk-off coordinate in the NOPA, which is expected to present the strongest spatio-temporal distortions or aberrations. The spatially resolved SPIDER measurements were performed placing a small aperture at different positions across the beam profile. To determine the position of the aperture relative to the near field intensity distribution, a flip-mirror was located before the input to the SPIDER to send the beam either to the SPIDER or to a CCD camera. At first, the near field distribution was recorded with the CCD camera. Then, the aperture was placed in the beam path, before the flip-mirror, and the CCD camera was utilized to locate the approximate position of the center of the aperture. Next, the mirror was removed from the beam path and the SPIDER trace recorded. The procedure was repeated for nine different positions. All the results of this section were taken at a repetition rate of 400 kHz, implementing pulse shaping and delay stabilization. Figure 6 shows the logarithm of the intensity distribution of the amplified pulses in the λ-x plane. The thickness of BBO 3 was 2 mm in this case and the output power after the chirped mirrors and a dichroic mirror to suppress the parasitic second harmonic was 4.8 W. It is worth mentioning that the intensity distribution in the imaging spectrograph is not corrected for the spectral response of the instrument.
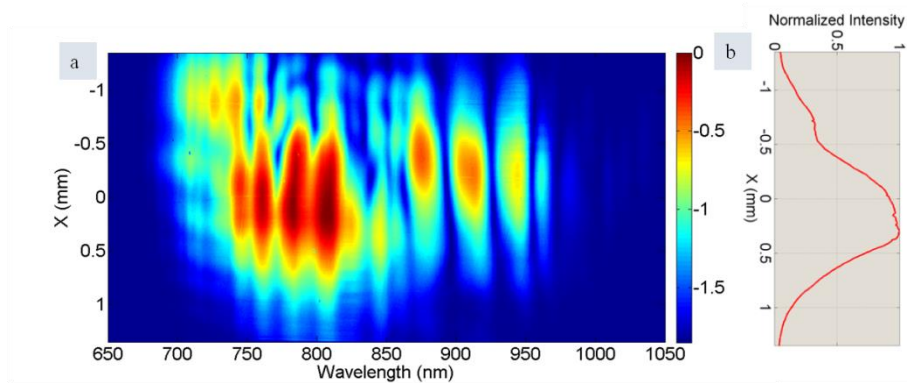
Fig. 6. (a) Logarithm of the normalized intensity distribution in the λ-x plane for the 4.8 W output. (b) Integration over wavelength of linear intensity distribution.

The intensity distribution in the λ-x plane shows a position-dependent spectrum, in particular in the wings of the beam. That is, within the full width at half maximum (FWHM) of the beam profile (along the x-axis, see Fig. 6(b)) the distribution does not change dramatically. There is however a shift in the center of gravity of the spectrum with position, slightly smaller than 20 nm/mm within the FWHM of the spatial distribution.

The intensity distribution from the imaging spectrograph is complemented by the spatially resolved SPIDER measurements. The results are shown in Fig. 7. Although the results of Figs. 6 and 7 correspond to the same NOPA configuration, the exact spectral shape is slightly different since the measurements were taken with a few days difference between them and the exact alignment and pump-seed delay might have changed. The graphs showing the spectra and the spectral phases are organized in a matrix consisting of three rows and three columns. The graph in the top-right corner corresponds to the top-right dot on the near field intensity distribution (Fig. 7(a)), etc. The same applies to the graphs showing the temporal pulse shapes. In all cases the difference of the spectral phase is shown with respect to the spectral phase in the center of the distribution. In this way the attention is focused on changes in the spectral phase relative to one point in the field distribution. Furthermore, in all the temporal shape reconstructions, the peak of the pulse has been arbitrarily located at time zero, eliminating all information concerning the group delay.

The results show that the changes in the spectral phase are not dramatic, although the pulse duration and shape are changing from point to point. The maximum difference in pulse duration with respect to the central position is as big as 29 %. This change is due not only to a position-dependent spectral phase, but also to changes in the spectral shape, leading to a longer transform-limited pulse duration. As expected, the changes are more evident across the x-axis, corresponding to the beams' walk-off axis in the NOPA.
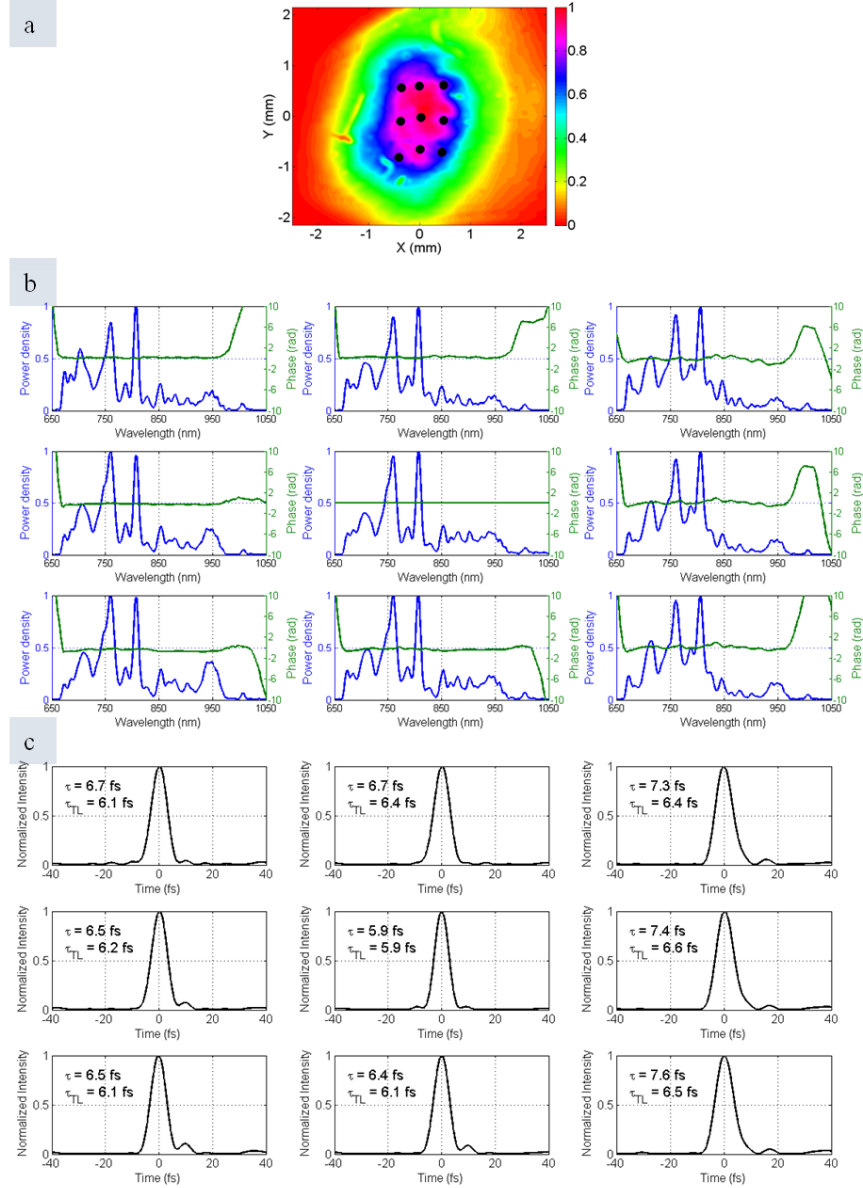
Fig. 7. Spatially-resolved SPIDER measurements for the 4.8 W output. (a) Near field distribution. The black dots indicate the position where the aperture was placed. (b) Measured spectra and spectral phase differences with respect to the spectral phase of the central point. (c) Retrieved temporal pulse shapes. There is a one-to-one correspondence between the positions of the dots on the near field distribution and the position of the spectrum or pulse shape in the 3 by 3 matrix of graphs.

A second set of measurements was performed running the NOPA under slightly different conditions. The last crystal (BBO 3 in Fig. 1(b)) was replaced by another BBO crystal with the same cut, but a thickness of 1.5 mm. The phase-matching angle, alignment and relative delay between pump and seed in the last crystal of the second stage were adjusted while monitoring the beam profile. The resulting intensity distribution in the λ-x plane is shown in

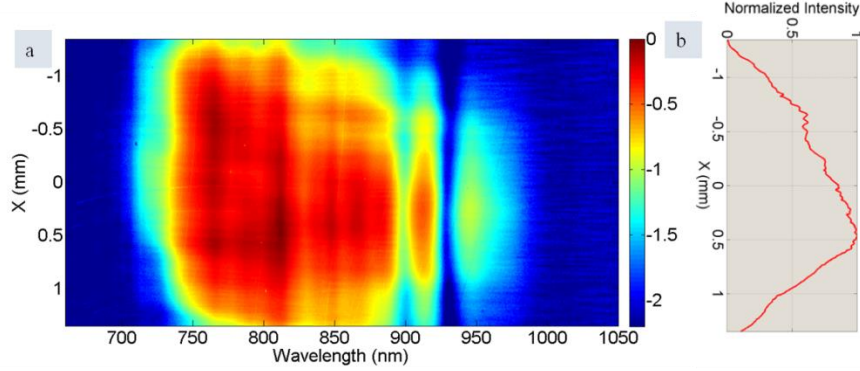Fig. 8. In this case the output power after filtering of the parasitic second harmonic was reduced to 4.4 W.

Fig. 8. (a) Logarithm of the normalized intensity distribution in the λ-x plane for a measurement with a 1.5 mm thickness for BBO 3 (4.4 W output). (b) Integration over the wavelength of the linear intensity distribution.

Although the spatio-spectral couplings are still present, the results in Fig. 8 show a much weaker dependence of the spectral shape on the position across the beam profile. In this case the shift in the center of gravity of the spectrum within the FWHM of the beam is smaller than 15 nm/mm. Again, this picture is complemented by spatially resolved SPIDER measurements, shown in Fig. 9.

The results in Fig. 9 still show a dependence of the pulse shape and spectral characteristics of the field with position. However the relative changes in the spectral phase and spectrum are smaller than in the previous case. The maximum difference in pulse duration amounts to 15 % of the pulse duration at the central location. In addition, the shape of the near field intensity distribution is symmetric with respect to the x- and y-axis, as opposed to the previous case where a weak tail extends to the positive side of the x-axis. Furthermore, as back-conversion effects are reduced at lower extraction efficiency, the spectral modulation in the amplified spectrum is also reduced and the satellite pulses in the transform-limited pulse shape are weaker, resulting in an improved temporal contrast.

The results presented in this section show that the spatio-temporal characteristics of the amplified pulses can be improved with only a mild decrease in the extraction efficiency (a reduction from 20% to 18%). However, the analysis presented so far does not address the amount of pulse front tilt and angular dispersion present in the near field distribution. It has been conclusively demonstrated experimentally, that the residual pulse front tilt induced by angular dispersion can be minimized by working at the magic angle configuration [40]. As explained in the same reference, the angular dispersion results from the angular dependent gain. This effect is particularly critical for small beams, when the angular acceptance of the amplifier is comparable to the beam angular range. For this reason, the non-collinear angle in the first amplification stage of our system was set to the magic angle. In the second amplifier however, the small non-collinear angle detuning is expected to induce a pulse front tilt. Following the results of [43], a pulse front tilt on the order of 0.7 fs/mm can be estimated at the output of the system (taking into account beam magnification), and a maximum pulse front tilt on the order of 2.1 fs/mm in the case that the detuning is as high as 0.3°. This was the case in [34], where a 2.2° non-collinear angle was utilized to obtain a broader bandwidth. For relatively large beams (when the angular acceptance of the amplifier is much bigger than the beam angular range), pulse front tilt can also originate as a consequence of the slanted gain produced by the two pulse fronts (pump and seed) subtending an angle (the non-collinear angle) [17, 41]. In this case pulse front tilt arises as a consequence of the simultaneous

presence of spatial and temporal chirp and can be minimized by introducing a controlled pulse front tilt in the pump pulse. The second stage of the NOPA described here, falls in a region with intermediate beam sizes, where other effects such as the walk-off between the beams may still play a significant role. Efforts to better understand this regime and other effects contributing to spatio-temporal distortions are underway. In addition, it is clear that a proper characterization of NOPAs requires describing the spatio-temporal properties of the amplified beams with devices offering spatially resolved spectral or temporal measurements such as the ones described in [44-47].
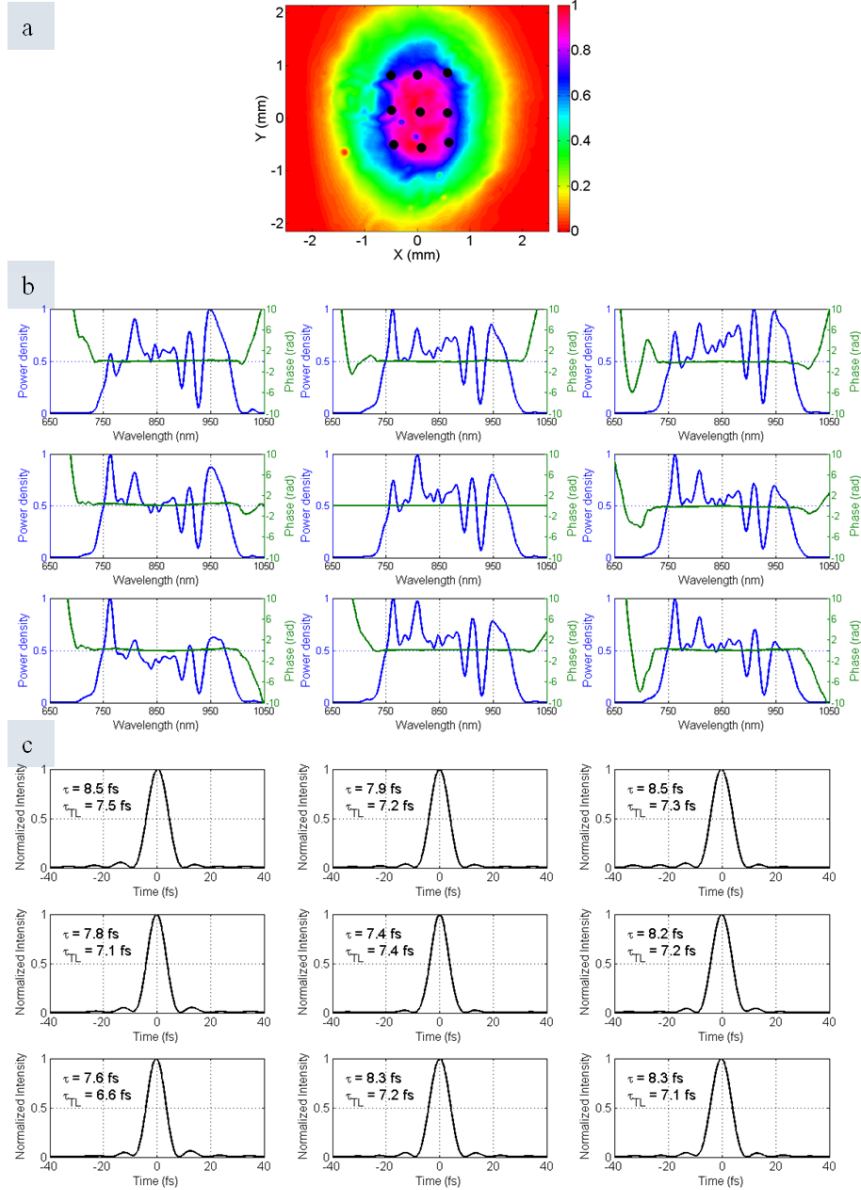

Fig. 9. Spatially-resolved SPIDER measurements for the 4.4 W output. (a) Near field distribution. The black dots indicate the position where the aperture was located. (b) Measured spectra and spectral phase differences with respect to the spectral phase of the central point. (c) Retrieved temporal pulse shapes.

6. Potential impact of spatio-temporal aberrations on applications

The results of section 5 and references therein, show that spatio-temporal distortions may not be negligible in many cases of interest. The importance of these effects will depend on the particular application to be considered. As a quantitative example of the impact of these distortions in experiments that are within the scope of interest of our research activities, an experiment on strong field ionization was simulated. Following the seminal work of Paulus and co-workers in [48], it is proposed as a thought experiment, studying the asymmetry in the number of photoelectrons emitted in opposite directions along the laser polarization for above-threshold ionization (ATI) with CEP-stable few-cycle pulses. This type of experiment is also known as stereo-ATI. As explained in [48], a considerable fraction of the electrons generated when atoms are exposed to intense laser fields, do not escape the atom directly, but rather return to the parent ion under the influence of the laser electric field, and are subject to an elastic collision with the ion and further acceleration by the laser field. These electrons form a plateau-like structure at high energies in the photoelectron kinetic energy spectrum (typically at energies between two times and ten times the ponderomotive energy of the free electrons -Up-) [49]. Moreover, only electrons generated within a small fraction of the laser half-cycle return to the ion core with high kinetic energy and are further accelerated by the laser field. This condition makes the plateau-electrons extremely sensitive to the exact temporal shape of the pulse, and therefore a good probe for CEP-effects and the exact spatio-temporal shape of the field.

To simulate the experiment, four different near field distributions were simulated for a collimated beam of 2 mm FWHM: I. ideal spectrum (constant spectrum across the beam profile) supporting 5 fs pulses combined with a constant spectral phase; II. position-dependent spectrum in which the center of gravity of the spectrum changes linearly with position at a rate of 30 nm/mm (i.e. spatial chirp), combined with a constant spectral phase; III. ideal spectrum combined with a position-dependent spectral phase in which the group delay changes linearly as a function of position (i.e. a pulse front tilt); IV. combination of pulse front tilt and spatial chirp.

The spatial chirp of 30 nm/mm represents an upper limit to the observed shifts in the center of gravity of the measured distributions in the λ-x plane that were reported in the previous section. The linear change in group delay with position that was chosen gives rise to a pulse front tilt of 2.8 fs/mm. This also corresponds to an upper limit for the angular dispersion induced pulse front tilt described in the previous section. Only angular dispersion-induced pulse front tilt was considered, since pulse front tilt arising from the combination of spatial and temporal chirp can be minimized when the pulses are compressed.

The ideal spectral distribution was built defining a super Gaussian spectrum of order 2 with a half width e^{-1} of 300 nm and centred at 850 nm. Eq. (1) shows the expression for the spectrum:

$$S(\lambda) = \left[e^{-(\lambda-\lambda_0)^2/\sigma^2} \right]^2 \tag{1}$$

In order for the spectrum to cover a realistic spectral range as compared to typical outputs of parametric amplifiers, the super Gaussian spectrum was multiplied by a spectral flat-top window extending from 650 nm to 1050 nm with super Gaussian edges of order 2 whose width are approximately 30 nm, i.e.

$$W(\lambda) = \begin{cases} \left[e^{-(\lambda-\lambda_1)^2/\sigma_1^2} \right]^2 ; \lambda < 650nm \\ 1; 650nm \leq \lambda \leq 1050nm \\ \left[e^{-(\lambda-\lambda_2)^2/\sigma_2^2} \right]^2 ; \lambda > 1050nm \end{cases} \tag{2}$$

where λ_1 = 650 nm, λ_2 = 1050 nm and $\sigma_1 = \sigma_2 \approx$ 30 nm. This spectrum gives rise to a transform-limited pulse duration of 4.97 fs. The spectrum was then multiplied by a Gaussian spatial function with a FWHM of 2 mm to build the distribution in the λ-x plane. For the distribution with spatial chirp, the same procedure was followed as for the ideal case, except that the central wavelength of the spectrum was changed with position at a rate of 30 nm/mm, and the width of the super Gaussian spectrum at each position was chosen such that the spectrum integrated over all positions had the same width at -10 dB as the ideal spectrum. In this case, the transform-limited pulse duration at the center of the beam was 5.10 fs.

For each near field spatio-spectral distribution, the electric field as a function of position and time was calculated, by means of the Huygens-Fresnel integral followed by inverse Fourier transform, approximately one Rayleigh length behind a focal plane. The focal distance was chosen so that the peak intensity reaches 10^{14} W/cm^2 in the interaction region, assuming a pulse energy of 10 µJ. Placing the interaction region one Rayleigh length away from the focal plane ensures that within the interaction volume where ionization takes place, the CEP along the propagation coordinate does not change substantially [50]. The next step was to solve the Time Dependent Schrödinger Equation (TDSE) for ionization of Argon utilizing the code described in [51]. The TDSE code assumes electric fields that are time-dependent but spatially homogeneous. In order to simulate spatial effects, a volume averaging has to be performed with a particular spatial distribution (a Gaussian beam for example). In this case, volume averaging was replaced by calculating the contribution to the photoelectron spectrum from each position across the spatial distribution. This was done at each position where the electric field was not negligible. All contributions were summed to obtain the angle-resolved photoelectron kinetic energy distribution. Figure 10(a) shows the energy- and angle-dependent distribution of photoelectrons for case I and a particular value of the CEP (0 radians). In the 2-dimensional graph of Fig. 10(a), a constant radius corresponds to constant kinetic energy (indicated in atomic units), while the angles (in degrees) indicate the emission angle of the photoelectrons with respect to the laser polarization. For better visualization, the logarithm of the distribution is shown in Fig. 10(a). For a given simulated distribution, two small angular slices (30°) were selected along the direction of the laser polarization (as indicated in Fig. 10(a)). Finally the number of plateau-like electrons with kinetic energy higher than 0.6 a.u. (= 2.4Up) within each angular slice was used to calculate an asymmetry parameter according to Eq. (3):

$$A = \frac{N_R - N_L}{N_R + N_L} \tag{3}$$

where $N_{R(L)}$ is the number of electrons flying to the right (left) along the laser polarization. The calculation was repeated for different values of the CEP and the parameter A was recorded as a function of the CEP (Fig. 10(b)).
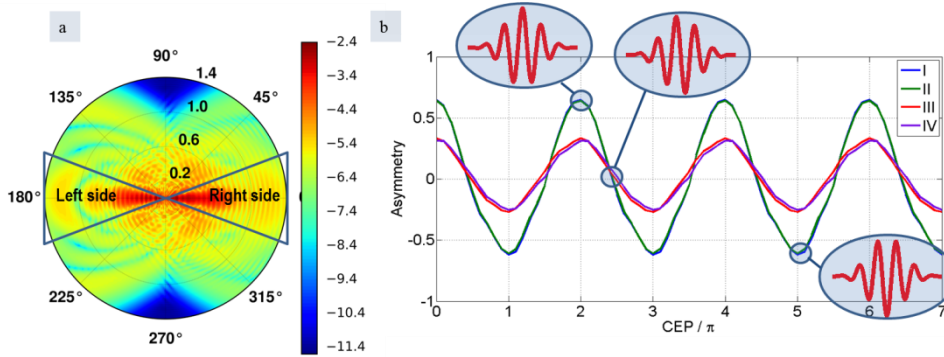
Fig. 10. (a) Calculated two-dimensional, angle-resolved photoelectron kinetic energy distribution plotted on a logarithmic color-scale. The angles are measured with respect to one direction along the laser polarization. The two angular regions utilized to calculate the asymmetry parameter are shown schematically. The different radii show different values of the kinetic energy in atomic units. Only electrons with kinetic energy higher than 0.6 atomic units were considered for the asymmetry calculation (b) Asymmetry parameter as a function of CEP for the four different field distributions described in the text. The three insets illustrate the temporal shape of the (ideal) electric field at different values of the CEP.

In the ideal case (I), the asymmetry oscillates with the CEP, as a result of the asymmetry in the shape of the electric field. This behavior is also observed almost unaltered when the spatio-temporal distortions comprise only a mild spatial chirp in the near field (case II). It is of course expected that for stronger spatial chirp the asymmetry is reduced. In the case that position-dependent spectral phase distortions are present in the near field, the results change dramatically. The amplitude of the oscillation in the asymmetry parameters reduces by more than 50 % in cases III and IV. Moreover, when integration is performed over the whole kinetic energy spectrum, the asymmetry reduces by an order of magnitude in cases III and IV as compared to cases I and II.

To better understand the origin of the loss of contrast in the modulation of the asymmetry parameter, the laser fields in the interaction region are examined in Fig. 11. The attention is focused on the electric fields derived from the near field distributions I (ideal case) and III (pulse front tilt). Distributions II and IV behave almost identical to I and III respectively. The time- and space-dependent electric fields are shown in Fig. 11(a) (for case I) and Fig. 11(b) (for case III), for a particular value of the CEP. It is quite clear from Fig. 11(a) that the temporal shape of the field, which ultimately determines the photoelectron asymmetry, remains almost unchanged with position for case I. This is further supported by Fig. 11(c) in which the electric field as a function of time is plotted for three different positions across the beam. For case III, Fig. 11(b) shows that the pulse front tilt is also present in the interaction region but more important, the field shape changes with position across the beam and the pulse duration is slightly longer, as it can be better observed in Fig. 11(d), which shows the electric field as a function of time at three different positions. The change in the shape of the electric field across the beam profile is quantified in Figs. 11(e) and 11(f), showing the asymmetry of the field temporal shape as a function of position for six different values of the CEP.
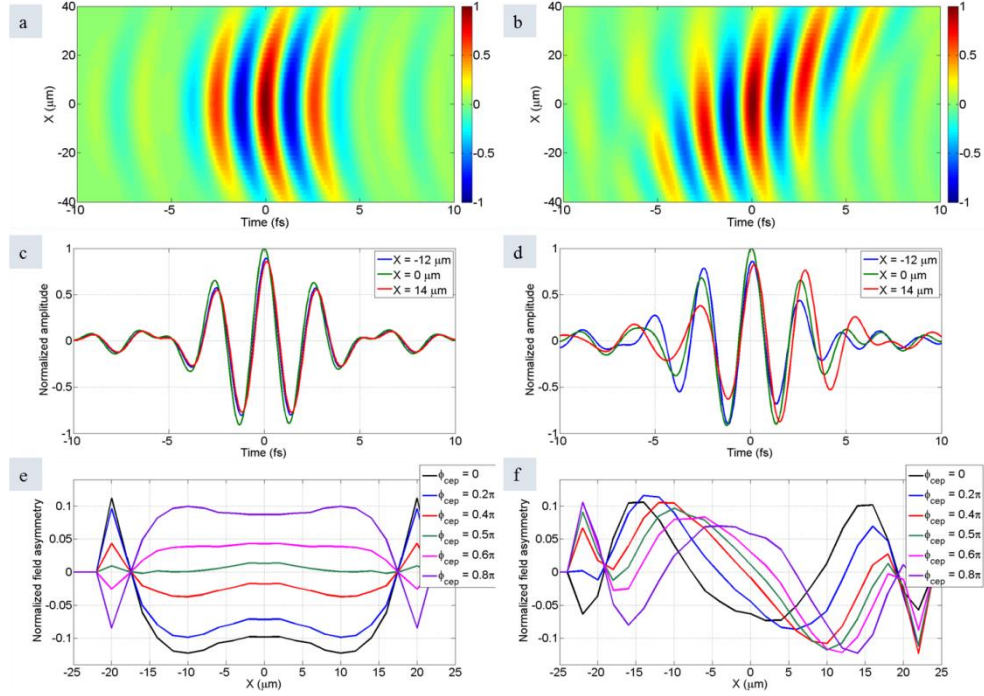
Fig. 11. Field temporal asymmetry in the interaction region for cases I (ideal) and III (pulse front tilt). (a) and (b) show the normalized electric field amplitude as a function of time and position for cases I and III respectively. (c) and (d) show the electric field amplitude as a function of time at three particular positions for cases I and III respectively. (e) and (f) quantify the temporal asymmetry of fields I and III respectively at different positions across the beam profile for different values of the CEP.

In Figs. 11(e) and 11(f), the normalized field asymmetry (*FA*) is quantified according to Eq. (4):

$$FA = \frac{1}{E_{max}(t_2 - t_1)} \int_{t_1}^{t_2} E(t)dt \qquad (4)$$

where E_{max} is the maximum field amplitude and the integration limits are chosen so that the field temporal asymmetry is calculated only within the region of the spatio-temporal distribution where the intensity is higher than half the peak intensity. This restricts the calculation at each position to a temporal window that comprises the strongest part of the pulse, and therefore the most relevant for determining the kinetic energy distribution of recollision electrons.

In case I (Fig. 11(e)) the field asymmetry remains relatively constant around the center of the beam (X = 0). Beyond X = ± 15 μm the value of the asymmetry changes drastically and even inverts its sign. However, the main contribution to the asymmetry in the photoelectron distribution in the plateau region comes from the strongest part of the field (i.e. around X = 0), where the field asymmetry remains relatively constant. In contrast to this, in case III (Fig. 11(f)) the field asymmetry changes more radically with position. Moreover, this change is not symmetric around the center of the beam. As a consequence, the asymmetry imprinted onto the photoelectrons depends strongly on where in the interaction volume the atom was ionized. After integration over the interaction volume, the net result is a weaker asymmetry of the total angle-resolved kinetic energy distribution.

The current example shows that for some often pursued applications in attosecond science spatio-temporal effects arising during non-collinear parametric amplification can substantially change the outcome of the experiment.

7.   Summary and perspectives

The high repetition rate NOPA introduced in [34] has been upgraded to deliver more than double the average power and energy per pulse, and has been optimized for applications. The pulse compression has been improved by means of a commercial pulse shaper acting on the NOPA seed, and the output power and spectral characteristics of the system have been stabilized over time by actively stabilizing the delay between the pump and seed pulses.

Additionally, the spatio-temporal properties of the amplified pulses have been studied in two configurations and the couplings or distortions have been minimized at the expense of conversion efficiency and a longer pulse duration.

Using the example of asymmetries in CEP-dependent above-threshold ionization, it was shown that even relatively weak spatio-temporal couplings may have detrimental effects for selected applications in attosecond science.

The results of these studies will have a strong impact on the design and development of a new high repetition rate NOPA currently under development. An order of magnitude higher energy per pulse is envisioned for this new system. This high energy, high repetition rate NOPA will be the corner stone of an attosecond beamline devoted to XUV-IR pump-probe spectroscopy experiments with coincidence detection.

Funding